Li Shi
e-mail: lishi@mail.utexas.edu
Department of Mechanical Engineering,
Center for Nano and Molecular Science and Technology,
University of Texas at Austin, TX 78712

Deyu Li
Department of Mechanical Engineering,
University of California, Berkeley, CA 94720

Choongho Yu
Department of Mechanical Engineering,
Center for Nano and Molecular Science and Technology,
University of Texas at Austin, TX 78712

Wanyoung Jang
Department of Physics,
Department of Mechanical Engineering,
University of California, Berkeley, CA 94720

Dohyung Kim
Department of Mechanical Engineering,
Center for Nano and Molecular Science and Technology,
University of Texas at Austin, TX 78712

Zhen Yao
Department of Physics,
Department of Mechanical Engineering,
University of California, Berkeley, CA 94720

Philip Kim
Department of Physics,
Columbia University, New York

Arunava Majumdar
Materials Science Division,
Lawrence Berkeley National Laboratory,
Department of Mechanical Engineering,
University of California, Berkeley, CA 94720

Measuring Thermal and Thermoelectric Properties of One-Dimensional Nanostructures Using a Microfabricated Device

We have batch-fabricated a microdevice consisting of two adjacent symmetric silicon nitride membranes suspended by long silicon nitride beams for measuring thermophysical properties of one-dimensional nanostructures (nanotubes, nanowires, and nanobelts) bridging the two membranes. A platinum resistance heater/thermometer is fabricated on each membrane. One membrane can be Joule heated to cause heat conduction through the sample to the other membrane. Thermal conductance, electrical conductance, and Seebeck coefficient can be measured using this microdevice in the temperature range of 4–400 K of an evacuated Helium cryostat. Measurement sensitivity, errors, and uncertainty are discussed. Measurement results of a 148 nm and a 10 nm-diameter single wall carbon nanotube bundle are presented. [DOI: 10.1115/1.1597619]

Keywords: Heat Transfer, Measurement Techniques, Microscale, Nanoscale, Thermoelectric

Introduction

One-dimensional (1D) nanostructures such as nanotubes, nanowires, and nanobelts have unique thermophysical properties very different from those of their bulk counter parts. In general, as these materials are confined to low dimensions with a size comparable to the scattering mean free paths, the thermal conductivity is often reduced due to increased boundary scattering and modified phonon dispersion [1,2]. An exception to this scaling trend is carbon nanotubes (CNs). Due to the unique crystalline structure, boundary scattering is nearly absent in CNs, giving rise to super high thermal and electrical conductivity that makes the CN an ideal candidate for nanoelectronic applications. Furthermore, a single wall (SW) CN is an ideal system to study quantum thermal conduction phenomena. For example, a (10,10) SWCN has a series of phonon sub-bands near the zone center [3]. The small diameter (d_t) of the nanotube causes relatively large sub-band splitting between the acoustic and the optical modes. For a temperature $T \ll 2hv/(k_B d_t)$, where h, v, k_B, d_t are Planck constant, phonon group velocity, Boltzmann constant, and tube diameter, respectively, only four acoustic modes are occupied, and the thermal conductance of a SWCN is expected to show linear temperature dependence with a maximum possible value $G_{th}=4g_0$. Here, $g_0=\pi^2 k_B^2 T/3h=(9.46\times10^{-13})T$ (W/K) is the universal quantum of thermal conductance [4].

The potential applications and intriguing nanoscale thermal conduction physics has inspired several groups to measure Seebeck coefficient [5], specific heat [6,7], and thermal conductivity [8,9] of CN bundles and mats. Hone et al. measured the thermal conductivity [7,8] and Seebeck coefficient [5] of millimeter size mat samples made of CNs. The measured thermal conductance shows linear temperature dependence below 25 K and extrapolates to zero at zero temperature. The measurement results have advanced our understanding of thermal conduction in CNs. However, it is difficult to extract the thermal conductivity of a single tube from such measurements because the sample consists of numerous micrometer-long tubes connected into a millimeter-size mat. As such, there exist large contact thermal resistances at the junctions between individual tubes in the mat. Further, the filling factor or density of the tubes in the mat is unknown. As the consequence, the estimated room-temperature thermal conductivity of

Contributed by the Heat Transfer Division for publication in the JOURNAL OF HEAT TRANSFER. Manuscript received by the Heat Transfer Division October 14, 2002; revision received April 8, 2003. Associate Editor: G. Chen.

the mat is about 250 W/m-K, one order of magnitude lower than theoretical predictions [10–12]. In addition, the measured thermal conductance increases with temperature for the entire temperature range of 8–350 K, showing no signature of Umklapp phonon-phonon scattering. This indicates that the dominant scattering mechanism is phonon scattering by defects and boundaries. Yi et al. [6] used a self heating 3ω method to measure the specific heat and thermal conductivity of a suspended millimeter-long aligned multi-wall (MW) CN bundle with an apparent cross section of 10^{-10} to 10^{-8} m^2. The measured specific heat exhibits linear temperature dependence in a temperature range of 10–300 K, showing a different behavior from the results obtained by Hone et al. In addition, because of the large thermal resistance at the defects and at the contacts between individual tubes, the measured thermal conductivity is about 20 W/m-K at room temperature, two orders of magnitude lower than theoretical predictions for a single defect-free tube.

It is necessary to investigate the intrinsic thermal transport properties of individual CNs by eliminating the influences from contact thermal resistances at the junctions between individual tubes and from phonon scattering between adjacent tubes. This is also the case for other nanostructures including a variety of nanotubes, nanowires, and nanobelts. Of particular interest, nanowires of Bi and Bi_2Te_3 may exhibit significant enhancement of the thermoelectric figure of merit, and have potential applications in efficient thermoelectric energy conversion [13,14]. Currently, there have been few measurement data of thermal properties of individual nanotubes, nanowires, and nanobelts. This is because conventional techniques for thin film thermal property measurements, such as the 3ω method [15], cannot be used readily for these nanostructures due to the small sample size. In order to concurrently measure thermal conductance, electrical conductance, and Seebeck coefficient of CNs, we and our collaborators developed a suspended microdevice in a previous work [16,17]. We used the device for measuring thermal conductivity and Seebeck coefficient of an individual suspended MWCN and obtained results in agreement with theory [17]. Here, we further optimize device design and fabrication process, improve the measurement method, and employ the technique for thermal property measurements of a variety of one-dimensional nanostructures. The following sections discuss the design, fabrication, measurement method, sensitivity, errors, and uncertainty of the technique. As a demonstration of the technique, the measurement results of two SWCN bundles are presented.

Experimental Methods

Device Design and Fabrication. Figure 1 shows a scanning electron micrograph (SEM) of the microdevice. The device is a suspended structure consisting of two adjacent 14 μm×25 μm low stress silicon nitride (SiN_x) membranes suspended with five 0.5-μm-thick, 420-μm-long and 2-μm-wide silicon nitride beams. One 30-nm-thick and 300-nm-wide platinum resistance thermometer (PRT) coil is designed on each membrane. The PRT is connected to 200 μm×200 μm Pt bonding pads on the substrate via 1.8 μm wide Pt leads on the long SiN_x beams. An additional 1.8 μm wide Pt electrode is designed on each membrane next to each other, providing electrical contact to the sample.

The device is batch fabricated using a wafer-stage microfabrication process, as shown in Fig. 2. First, a 0.5-μm-thick low-stress SiN_x film is deposited on a 100-mm-diameter wafer using a low pressure chemical vapor deposition (LPCVD) method, as shown in Fig. 2(a). A 30 nm-thick Pt film is then deposited on the SiN_x film by radio-frequency (RF) sputtering. A 300-nm-thick low temperature silicon dioxide (LTO) is grown on the Pt film using LPCVD. A photoresist is spun on the LTO film and patterned using an I-line wafer stepper. Combined with an oxygen plasma etching technique, the wafer stepper can produce photoresist patterns with a line width below 0.4 μm. The photoresist pattern is then transferred to the LTO film using reactive ion etching (RIE).

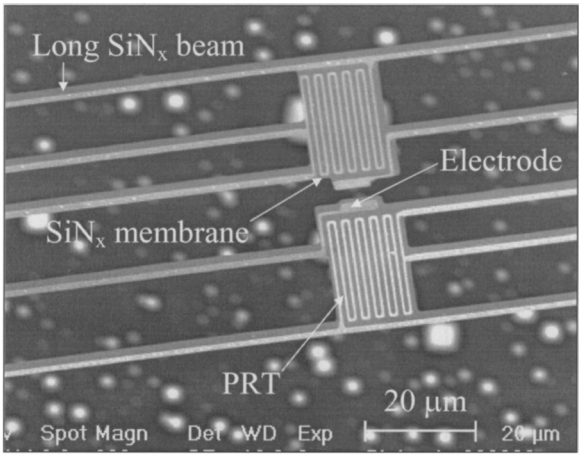

Fig. 1 SEM micrograph of a microdevice for thermal property measurements of nanostructures

Using the patterned LTO as a mask, the unprotected Pt film is etched using ion milling or sputter etching to make serpentine PRT lines (Fig. 2(b)). After the photoresist and LTO are stripped, a 300-nm-thick LTO is deposited on the wafer. A photolithography and wet etching step is then used to open contact windows to the Pt contact pads for wire bonding, and to the 1.8 μm wide Pt electrode near the PRT. This Pt electrode is used for making electrical contact to the sample. A photoresist film is then spun on the wafer and patterned (Fig. 2(c)). The pattern is transferred to the SiN_x film by RIE. After the photoresist is stripped, tetramethylammonium hydroxide (TMAH) is used to etch the exposed Si region and the suspended structure is released when the Si substrate is etched away, as shown in Fig. 2(e). The etching pit in the Si substrate is usually about 100–200 μm deep, and as such the

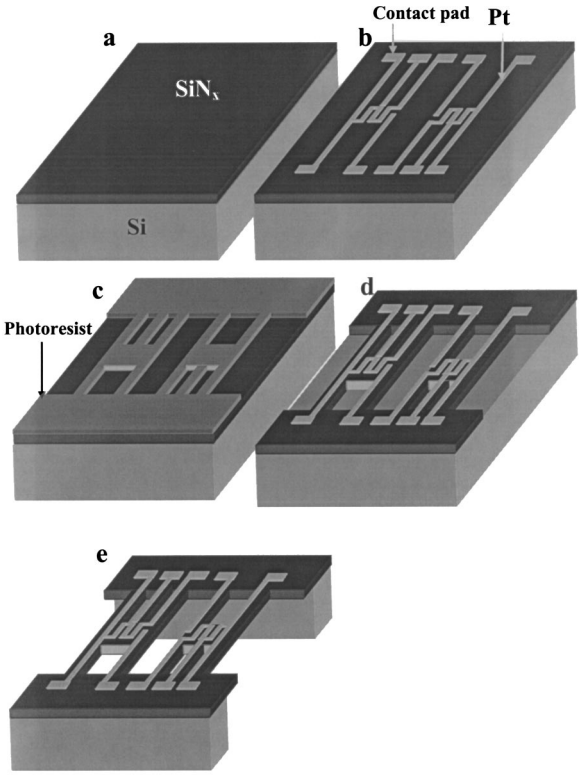

Fig. 2 Fabrication process of the microdevice

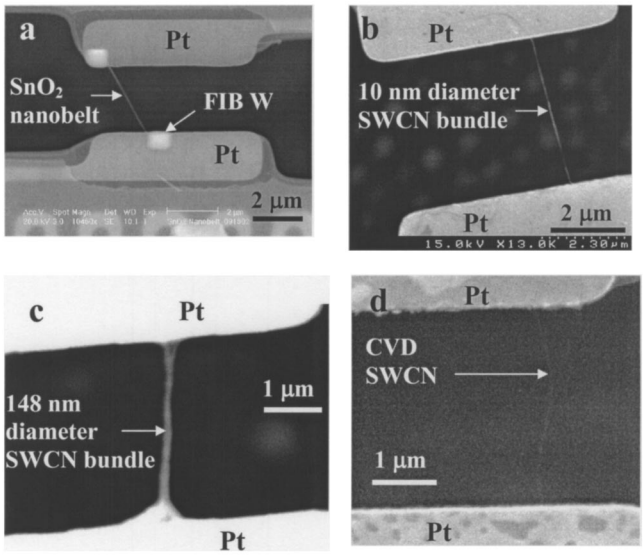

Fig. 3 SEM image of a SnO_2 nanowire (a), a 10 nm diameter SWCN bundle (b), a 148 nm diameter SWCN bundle (c), and a CVD-grown SWCN (d) connecting two Pt electrodes on two suspended membranes

suspended structure does not collapse to the substrate even without the use of a critical point dryer. Using this wafer-stage fabrication technique, about 2000 densely packed suspended structures can be made on a 100 mm diameter wafer.

A nanotube, nanowire, or nanobelt can be placed between the two suspended membranes by several methods. One way is to use a sharp probe to pick up a sample, and then manipulate the probe using a probe station to place the sample between the two membranes. The process requires a high-resolution optical microscope. This method was employed in our previous work for placing MWCN bundles and individual MWCNs between two membranes [17].

The probe manipulation method is a tedious process. In view of this, we have developed two different approaches for trapping a nanostructure sample between the two membranes. In the first approach, a solution containing the nanostructures is dropped and spun on a wafer containing many suspended devices. We have found that the nanostructures are often adsorbed on the two Pt electrodes. Figures 3(a–c) show a SnO_2 nanobelt, a 10 nm diameter SWCN bundle, and a 148 nm diameter SWCN bundle adsorbed on the two membranes, respectively, by this wet deposition method. To improve the thermal and electrical contact between the sample and the Pt electrode, we usually anneal the device at 300°C for a few hours. Further, a small tungsten or Pt pad can be deposited on top of the sample-electrode contact using a focused ion beam technique, as shown in Fig. 3(a). Alternatively, an amorphous carbon film can be deposited on top of the sample-electrode contact region. To do that, the electron beam of a SEM is focused on the contact region with a high magnification of 200,000 or larger. Because of organic contamination in the SEM chamber, the electron beam induces the deposition of a carbon film on the focused region. This can further improve the contact.

In the second approach, we employ a chemical vapor deposition (CVD) method to grow individual SWCNs bridging the two membranes. To do that, we first spin a solution containing catalyst nano-particles made of Fe, Mo, and Al_2O_3 on the suspended membranes. This yields many catalyst nano-particles deposited on the Pt electrodes. The suspended device is then placed in a 900°C CVD tube with flowing methane resulting in individual SWCNs grown between two catalyst particles on the two Pt electrodes. Figure 3(d) shows a SWCN synthesized by this method. The sample-electrode contact is annealed in the high-temperature growth process, leading to low contact resistances.

Measurement Method

Thermal Conductance. Figure 4 shows the schematic diagram of the experimental setup for measuring the thermal conductance of the sample. The suspended structure is placed in a cryostat with a vacuum level better than 1×10^{-5} Torr. The two suspended membranes are denoted as the heating membrane and sensing membrane, respectively. A dc current (I) flows to one of the two PRTs. A Joule heat $Q_h=I^2R_h$ is generated in this heating PRT that has a resistance of R_h. The PRT on each membrane is connected to the contact pads by four Pt leads, allowing four-probe resistance measurement. The resistance of each Pt lead is R_L, which is about half of R_h. A Joule heat of $2Q_L=2I^2R_L$ is dissipated in the two Pt leads that supply the dc current to the heating PRT. We assume that the temperature of the heating membrane is raised to a uniform temperature T_h. This assumption can be justified because the internal thermal resistance of the small membrane is much smaller than the thermal resistance of the long narrow beams thermally connecting the membrane to the silicon chip at temperature T_0. A certain amount of the heat (Q_2) is conducted through the sample from the heating membrane to the sensing one, raising the temperature of the latter to T_s. In vacuum and with a small $\Delta T_h(\equiv T_h-T_0<6$ K), the heat transfer between the two membranes by air conduction and radiation is negligible compared to Q_2, as discussed below. The heat flow in the amount of Q_2 is further conducted to the environment through the five beams supporting the sensing membrane. The rest of the heat, i.e., $Q_1=Q_h+2Q_L-Q_2$, is conducted to the environment through the other five beams connected to the heating membrane.

The five beams supporting each membrane are designed to be identical. It can be shown that below 400 K, the radiation and air conduction heat losses from the membrane and the five supporting beams to the environment are negligible compared to conduction heat transfer through the five beams. Hence, the total thermal conductance of the five beams can be simplified as $G_b=5k_lA/L$, where k_l, A, and L are the thermal conductivity, cross

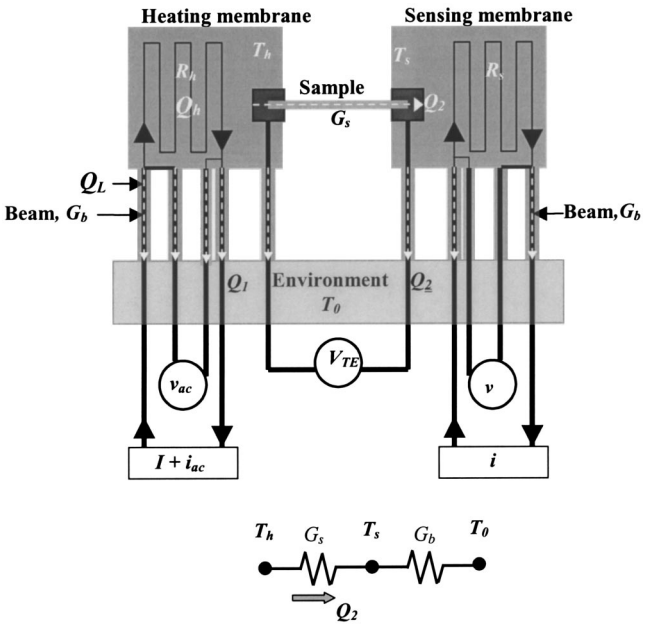

Fig. 4 Schematic diagram and thermal resistance circuit of the experimental setup

sectional area, and length of each beam, respectively. We can obtain the following equation from the thermal resistance circuit shown in Fig. 4,

$$Q_2 = G_b(T_s - T_0) = G_s(T_h - T_s), \tag{1}$$

where G_s is the thermal conductance of the sample and consists of two components, i.e.,

$$G_s = (G_n^{-1} + G_c^{-1})^{-1} \tag{2}$$

where $G_n = k_n A_n / L_n$ is the intrinsic thermal conductance of the nanostructure, k_n, A_n, and L_n are the thermal conductivity, cross sectional area, and length of the free-standing segment of the sample between the two membranes, respectively. G_c is the contact thermal conductance between the nanostructure and the two membranes. Because the temperature excursion ΔT_h is small, G_s, G_b, and G_c are assumed to be constant as ΔT_h is ramped.

Considering one-dimensional heat conduction, one can obtain temperature distribution in the ten beams supporting the two membranes. A Joule heat of Q_L is generated uniformly in each of the two Pt leads supplying the heating current, yielding a parabolic temperature distribution along the two beams; while linear temperature distribution is obtained for the remaining eight beams without Joule heating. The heat conduction to the environment from the two Joule-heated beams can be derived as $Q_{h,2} = 2(G_b \Delta T_h/5 + Q_L/2)$; while that from the remaining three beams connected to the heating membrane is $Q_{h,3} = 3G_b \Delta T_h/5$, and that from the five beams connected to the sensing membrane is $Q_{s,5} = G_b \Delta T_s$, where $\Delta T_s \equiv T_s - T_0$. Considering energy conservation, i.e., $Q_{h,2} + Q_{h,3} + Q_{s,5} = Q_h + 2Q_L$, one obtains

$$G_b = \frac{Q_h + Q_L}{\Delta T_h + \Delta T_s}, \tag{3a}$$

and

$$G_s = G_b \frac{\Delta T_s}{\Delta T_h - \Delta T_s}. \tag{3b}$$

Q_h and Q_L can be calculated readily from the dc current and the voltage drops across the heating PRT and the Pt leads. ΔT_h and ΔT_s are calculated from the measured resistance of the two PRTs and their temperature coefficient of resistance (TCR $\equiv (dR/dT)/R$). The four-probe differential electrical resistance R_s of the sensing PRT is measured using a SR830 lock-in amplifier with a 250–500 nA, 199 Hz sinusoidal excitation current. The temperature rise ΔT_s of the sensing membrane depends on the DC current I of the heating PRT, and is related to R_s according to the following equation

$$\Delta T_s(I) = \frac{\Delta R_s(I)}{\dfrac{dR_s(I=0)}{dT}}; \quad \Delta R_s(I) \equiv R_s(I) - R_s(I=0) \tag{4}$$

The differential resistance R_h of the heating PRT can be obtained by one of the two following methods. In the first method, the $I-V$ curve is measured as the dc current (I) is slowly ramped up to a value in the range of 4–10 μA depending on T_0. One ramping cycle typically takes 15 minutes. The *differential* resistance of the PRT heater is calculated as $R_h = dV/dI$. For a slow voltage ramp rate, it can be shown that the temperature rise in the heating membrane is

$$\Delta T_h(I) = \frac{\Delta R_h(I)}{3\dfrac{dR_h(I=0)}{dT}}; \quad \Delta R_h(I) \equiv R_h(I) - R_h(I=0) \tag{5}$$

Here, we use the differential resistance instead of the average resistance ($\equiv V/I$) because the former offers better sensitivity for temperature measurement.

Alternatively, a 250–500 nA sinusoidal current (i_{ac}) with a frequency f can be coupled to the much larger dc heating current I. A SR830 lock-in amplifier is used to measure the first harmonic component (v_{ac}) of the voltage drop across the heating PRT, yielding the differential resistance $R_h = v_{ac}/i_{ac}$. For R_h obtained by this method, it can be shown that

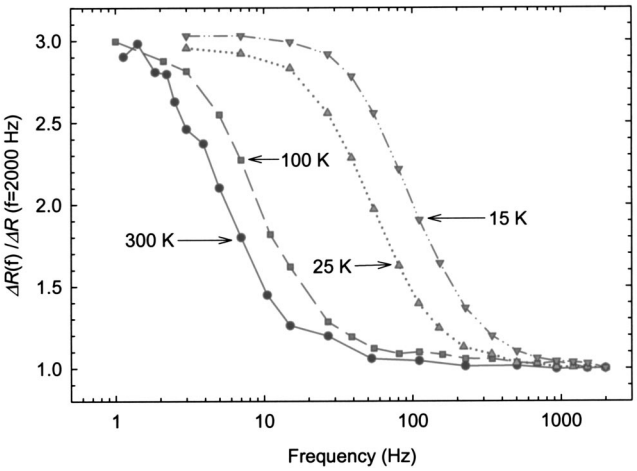

Fig. 5 Normalized first harmonic component of the measured resistance rise of the heating PRT as a function of the frequency of an ac current coupled to the dc heating current

$$\Delta T_h(I) = \frac{\Delta R_h(I)}{3\dfrac{dR_h(I=0)}{dT}}, \quad \text{for } f \ll 1/(2\pi\tau) \tag{6a}$$

$$\Delta T_h(I) = \frac{\Delta R_h(I)}{\dfrac{dR_h(I=0)}{dT}}, \quad \text{for } f \gg 1/(2\pi\tau) \tag{6b}$$

where τ is the thermal time constant of the suspended device, and is estimated to be on the order of 10 ms. The difference between these two solutions origins from a first harmonic modulated heating component, i.e., $2i_{ac}IR_h$. At a very low (high) frequency compared to $1/(2\pi\tau)$, the modulated heating yields a nontrivial (trivial) first harmonic component in T_h. This further causes a nontrivial (trivial) first harmonic oscillation in R_h. This effect gives rise to the factor of 3 difference between Eq. 6(a) and Eq. 6(b). In addition, τ is proportional to C/k, where C and k are the heat capacity and thermal conductivity, respectively. According to the kinetic theory, k is proportional to Cl, where l is the phonon mean free path and increases with decreasing temperature. Hence, τ is proportional to $1/l$ and decreases with decreasing temperature. Therefore, the transition between Eq. 6(a) and Eq. 6(b) occurs at a higher frequency as the temperature is lowered. This frequency dependence has been confirmed by an experiment conducted at four different temperatures, namely 15 K, 25 K, 100 K, and 300 K, as shown in Fig. 5. In the experiment, ΔR_h was measured at different f for the same I (thus the same ΔT_h). The measurement results exhibit a factor of 3 difference between the low and high frequency limits, as expected from Eq. 6. In practice, we use $f > 700$ Hz, for which Eq. 6(b) is valid in the temperature range of 4−400 K. We confirmed that the lock-in method yields the same result as the fitting method. The lock-in method is preferred in our measurements because it is more sensitive than the fitting one.

Electrical Conductance. The electrical conductance of the sample can be measured using the two Pt electrodes contacting the two ends of the sample. As mentioned above, a FIB method can be used to deposit a metal line on top of the sample-electrode contact to reinforce the electrical contact and minimize the contact

electrical resistance. The FIB deposition can break through the oxide layer of a semiconductor nanowire and reduce the contact resistance.

Seebeck Coefficient. The temperature difference of the two membranes yields a thermoelectric voltage that can be measured using the two Pt electrodes contacting the nanostructure, i.e., $V_{TE}=(S_s-S_{Pt})(T_h-T_s)$. The Seebeck coefficient (S_{Pt}) of the Pt electrode can be calibrated separately. By measuring T_h, T_s, and V_{TE}, the Seebeck coefficient (S_s) of the sample can be obtained.

Measurement Sensitivity. The sensitivity of thermal conductance measurement determines the minimum or noise-equivalent sample thermal conductance that can be measured using the microdevice. Usually $\Delta T_h \gg \Delta T_s$ in our measurements. Hence, from Eq. 3(b), the noise-equivalent thermal conductance (NEG_s) of the sample is proportional to the noise-equivalent temperature rise (NET) of the sensing membrane, i.e.

$$\mathrm{NEG}_s = G_b \frac{\mathrm{NET}}{\Delta T_h - \Delta T_s} \tag{7}$$

NET is further related to the noise equivalent resistance (NER) in the R_s measurement

$$\mathrm{NET} = \frac{\mathrm{NER}/R_s}{\mathrm{TCR}} \tag{8}$$

For the resistance measurement method using a lock-in amplifier,

$$\frac{\mathrm{NER}}{R_s} = \frac{\delta v}{v} + \frac{\delta i}{i} \tag{9}$$

where δv and δi are the noises in the ac voltage measurement and that of the current source, respectively. At 300 K, δv is dominated by the thermal or Johnson noise to be $\delta v = \sqrt{4k_B T R_s \Delta f} \approx 4$ nV for a noise bandwidth of $\Delta f \approx 0.3$ Hz. Therefore

$$\frac{\delta v}{v} = \frac{4\ \mathrm{nV}}{2\ \mathrm{mV}} = 2\times 10^{-6} \tag{10}$$

The current source $i = v_{\mathrm{out}}/R$, where v_{out} is a sinusoidal 199 Hz output voltage from the lock-in amplifier and R is the 10 MΩ resistance of a 10 ppm/K precision resistor that is coupled to the sinusoidal voltage output of the lock-in amplifier for converting a constant ac voltage source to a constant ac current source. Therefore,

$$\frac{\delta i_{ac}}{i_{ac}} = \frac{\delta v_{\mathrm{out}}}{v_{\mathrm{out}}} + \frac{\delta R}{R} \tag{11}$$

The relative noise in the ac voltage output from the lock-in amplifier ($\delta v_{\mathrm{out}}/v_{\mathrm{out}}$) is about 4×10^{-5}. The resistance fluctuation ($\delta R/R$) of the 10 MΩ precision resistance is about 2×10^{-6} for a 0.2 K fluctuation of room temperature. Therefore, $\delta i_{ac}/i_{ac} \sim 4.2 \times 10^{-5}$. The noise in the current source is the dominant noise source. From Eqs. 9–11, we can write

$$\frac{\mathrm{NER}}{R_s} \approx 5\times 10^{-5} \tag{12}$$

This has been confirmed by measuring the noise level using a 2 KΩ precision resistor to replace the PRT. The measured resistance noise is about 100 mΩ, indicating $\mathrm{NER}/R_s \approx 5\times 10^{-5}$.

$R_s(I=0)$ is measured in the temperature range of 10–400 K, as shown in Fig. 6. Above 30 K, $R_s(I=0)$ increases linearly with temperature. Typically, the TCR of the PRT is in the range of 1.8×10^{-3}–3.6×10^{-3} K^{-1} and 3.5×10^{-3}–7.2×10^{-3} K^{-1} at 300 K and 30 K, respectively, depending on the thin film deposition condition. Thus, NET of the lock-in measurement is in the range of 13–27 mK and 6–13 mK at 300 K and 30 K, respectively. Below 30 K, the TCR becomes smaller, leading to a larger NET.

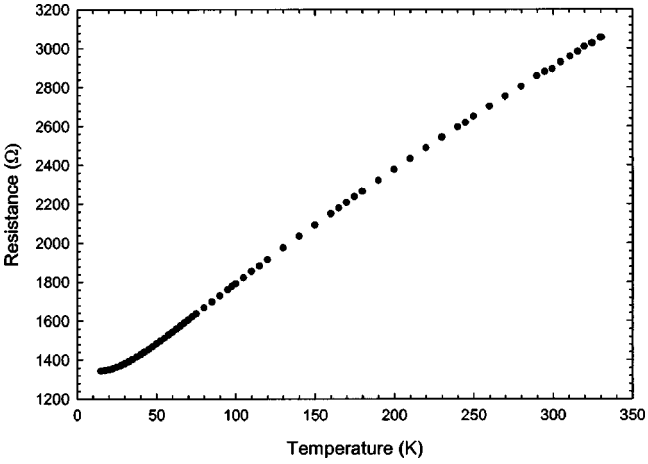

Fig. 6 The resistance ($R_s(I=0)$) of the PRT as a function of temperature

This NET value was found to be comparable or slightly below the temperature fluctuation of the cryostat, which can be controlled to be within 25 mK for $T_0 > 100$ K and 10 mK for $T_0 < 100$ K. Therefore,

$$\mathrm{NET} \approx 25\ \mathrm{mK} \quad \text{for } T_0 = 300\ \mathrm{K};$$
$$\mathrm{NET} \approx 10\ \mathrm{mK} \quad \text{for } T_0 = 30\ \mathrm{K} \tag{13}$$

The thermal conductance (G_b) of the five beams has been calculated from the measured ΔT_h and ΔT_s according to Eq. 3(a). The measured ΔT_h is shown in the inset of Fig. 7 as a function of I, and the calculated G_b is shown in Fig. 7. At 300 K, G_b is about 9.4×10^{-8} W/K, in agreement with the value of 9.0×10^{-8} W/K that is obtained based on the geometry of the five beams as well as the room temperature thermal conductivity values of SiN_x and Pt films, i.e., $k_{\mathrm{SiNx}} = 5.5$ W/m-K and $k_{\mathrm{Pt}} = 70$ W/m-K [16]. Therefore, from Eqs. 7 and 13, the noise equivalent thermal conductance at 300 K is $NEG_s \approx 1\times 10^{-9}$ W/K for a temperature excursion $\Delta T_h - \Delta T_s = 2$ K. At 30 K, $G_b \approx 3\times 10^{-8}$ W/K, and $NEG_s \approx 1.5 \times 10^{-10}$ W/K for the same temperature excursion. If only the four acoustic phonon modes are filled up for a (10,10) SWCN at 30 K, the maximum possible thermal conductance would be $G_{SWCN} = 4g_0 = 4\times 30\times 9.46\times 10^{-13}\ \mathrm{W/K} = 1.1\times 10^{-10}$ W/K. This is in

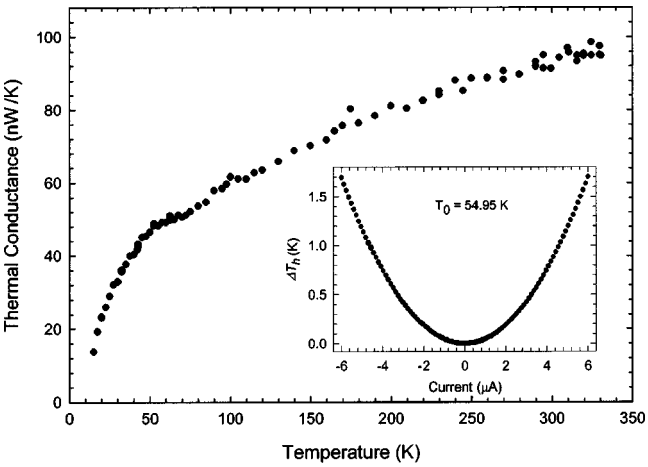

Fig. 7 Thermal conductance of the five beams supporting one membrane of the microdevice as a function of temperature. Inset: temperature rise in the heating membrane as a function of the dc heating current at $T_0 = 54.95$ K.

the vicinity of the measurement sensitivity. To increase the signal to noise ratio, two or more individual SWCNs can be grown between the two suspended membranes using the CVD method, or an Nb doped Si resistance thermometer with a larger TCR [18] can be used to replace the PRT.

Measurement Errors. One error source of the measurement is due to heat transfer between the two membranes via radiation and air conduction. The radiation thermal conductance can be estimated as

$$G_{h-s\_\mathrm{rad}}=\sigma(T_s+T_h)(T_s^2+T_h^2)F_{h-s}A \tag{14}$$

where F_{h-s} and A are the view factor between the two adjacent membranes and the surface area of one membrane, respectively. It can be shown that $F_{h-s}A\approx 12\,\mu\mathrm{m}^2$. Thus $G_{h-s\_\mathrm{rad}}=8\times10^{-14}$ and 7×10^{-11} W/K at $T=30$ K and 300 K, respectively. These values are well below the measurement sensitivity.

The thermal conductance of air can be written as $G_{h-s\_\mathrm{air}}=k_aA_{eq}/D$, where k_a is the thermal conductivity of the residual air molecules in the evacuated cryostat, A_{eq} and D are the equivalent surface area of the membrane and the distance between the two membranes, respectively. For a vacuum pressure of 1×10^{-5} Torr, the mean free path of air molecules is of the order of 1 m and is much larger than D. Under such circumstance, according to the kinetic theory,

$$k_a=\frac{CvD}{3} \quad \text{and} \quad G_{h-s\_\mathrm{air}}=\frac{CvA_{eq}}{3} \tag{15}$$

where C and v are the heat capacity and velocity of air molecules. From Eq. 15, it can be estimated that $G_{h-s\_\mathrm{air}}=2\times10^{-12}$ W/K at $T=300$ K, well below the measurement sensitivity of 1×10^{-9} W/K.

We have measured the thermal conductance due to air conduction and radiation at different temperatures using a bare device without a nanostructure sample bridging the two membranes. No signal above the noise level can be detected by the sensing PRT as the temperature of the heating membrane is raised. The measurement confirms that air conduction and radiation do not introduce noticeable errors in our measurements.

A major error source in the measurement is the contact thermal resistance (G_c^{-1}). To decrease G_c^{-1}, as discussed in the previous section, one can deposit a small Pt or W pad on top of the sample-electrode contact so that the sample is sandwiched between two metal layers. Alternatively, amorphous carbon can be deposited on the contact area using a SEM. Note that the contact area between the sample and the electrode is proportional to the diameter of the nanostructure sample; while the thermal conductance of the sample is proportional to the square of the diameter. Therefore, as a general trend, the ratio of G_c to G_n is larger as the diameter of the sample becomes smaller. For this reason, the contact thermal resistance causes a smaller error at nanoscale than at macroscale.

In a measurement of Si nanowires, we estimated the error introduced by the contact thermal resistance. In that measurement, amorphous carbon was deposited on the contact area. The conductance of one of the contacts can be expressed as k_cA_c/δ_a, where k_c is the thermal conductivity of the amorphous carbon; A_c is the contact area and is of the order of $2\pi rL_c$, where L_c is the length of the carbon deposit (about 2 μm), and r is the radius of the nanowire; δ_a is the average distance between the nanowire surface and Pt electrode, which is of the order of r. Using $k_c=0.1$ W/m-K, the lower limit of inorganic solid materials, and $k_n=47$ W/m-K, the room temperature measurement value of a 100 nm diameter Si nanowire, we estimated that $G_c/G_n=6.8$. Hence, the two contacts together yielded an error less than 15 percent for the 100 nm Si nanowire. This error is expected to be smaller for nanowires with a smaller diameter.

Nevertheless, it is desirable to quantify the contact thermal resistance G_c. A conventional method is to measure a collection of samples with the same diameter and different lengths. The contact thermal resistance can be estimated from the length-dependence of the sample thermal conductance (G_s) provided that thermal conduction in the sample is diffusive.

Table 1 Uncertainty of thermal conductance (G_s) data shown in Fig. 8

Temperature (K)	300	160	30
148 nm diameter SWCN bundle	9%	14%	36%
10 nm diameter SWCN bundle	36%	57%	···

Measurement Uncertainty. For the case when $\Delta T_h \gg \Delta T_s$ the uncertainty of the measured thermal conductance of the sample can be written as

$$\frac{\delta(G_s)}{G_s}=\frac{\delta(Q)}{Q}+\frac{\delta(\Delta T_s)}{\Delta T_s}+2\,\frac{\delta(\Delta T_h)}{\Delta T_h} \tag{16}$$

where $\delta(x)$ is the uncertainty in x. Since $\Delta T_h \gg \Delta T_s$, the dominant term in the left hand side of Eq. 16 is $\delta(\Delta T_s)/\Delta T_s$. With $\mathrm{d}R_s(\mathrm{I}=0)/\mathrm{d}T$ obtained from Fig. 6 and considering a 1 percent gain accuracy of the lock-in amplifier, we estimated from Eq. 4 that the upper limit of $\delta(\Delta T_s)$ is 36 mK. Further, ΔT_s depends on G_s/G_b. When measuring the 148 nm diameter SWCN bundle shown in Fig. 3(c), we increased ΔT_h up to 2 K. It was found that $G_s\approx0.2G_b$ at 300 K. Hence, $\Delta T_s(\approx\Delta T_hG_s/G_b)$ was as high as 0.4 K, and $\delta G_s/G_s\approx\delta(\Delta T_s)/\Delta T_s\approx9$ percent at 300 K. At 30 K, $G_s\approx0.05G_b$, so that $\Delta T_s\approx0.1$ K. This results in $\delta G_s/G_s\approx\delta(\Delta T_s)/\Delta T_s\approx36$ percent at 30 K. For the 10 nm diameter SWCN bundle shown in Fig. 3(b), we increased ΔT_h up to 6 K in order to keep the uncertainty $\delta G_s/G_s$ below 36 percent and 57 percent at 300 K and 160 K, respectively. These uncertainty values, as summarized in Table 1, represent the upper bound because they are estimated using the upper limit of $\delta(\Delta T_s)$.

To obtain the thermal conductivity, one needs to measure the length and diameter of the sample. The length of the sample can be measured using a SEM with a uncertainty of 10 nm. Thus, for a 2 μm long sample, $\delta(L)/L=0.5$ percent. To obtain the diameter, we used a tapping mode atomic force microscope to measure the sample segment that is located on top of the Pt electrode. The uncertainty of the diameter measurement was about 0.3 nm. For the 10 nm (or 148 nm) diameter SWCN bundle, this introduces an additional uncertainty of 6 percent (or 0.4 percent) to the calculated thermal conductivity. These uncertainty values are usually smaller than that introduced by the uncertainty of G_s. However, the calculated thermal conductivity (k) does not take into account of the contact thermal resistance (G_c), and thus represents the lower bound of k.

Measurement Results and Discussion

Using the microdevice, a variety of nanostructure samples have been measured. These include MWCNs [17], SWCNs, nanowires made of Si [19] and Bi_2Te_3 [20], and SnO_2 nanobelts [21]. It exceeds the scope of this paper to include all the measurement results. For appropriate nanostructures of interest, the readers are referred to the appropriate papers cited in the reference section.

As an example, Figs. 8–10 show the measurement results of thermal conductance, electrical conductance, and Seebeck coefficient of a 10 nm diameter and 4.2 μm long SWCN bundle (see Fig. 3(b)) and another 148 nm diameter, 2.66 μm long SWCN bundle (see Fig. 3(c)). For the 148 nm diameter bundle, the thermal conductance exhibits a $T^{1.5}$ dependence between 20 K and 100 K. This is different from the quadratic temperature dependence observed for individual MWCNs [17] as well as the linear dependence observed by Hone et al. for a SWCN mat below 25 K. To verify the expected linear behavior expected for SWCNs at low temperatures, we will need to measure individual SWCNs grown by the CVD method in order to eliminate the influences

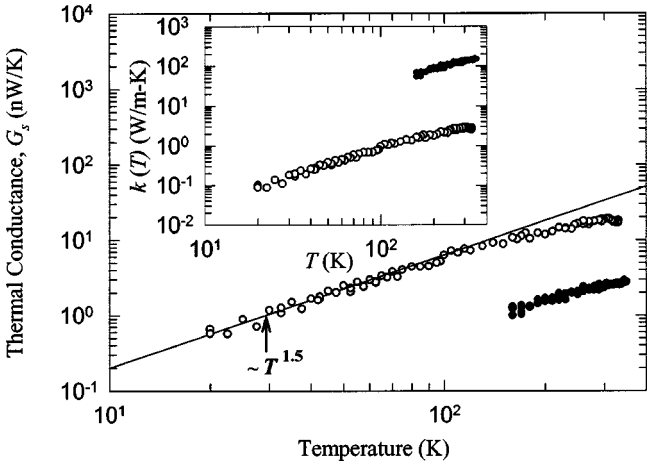

Fig. 8 Thermal conductance of two SWCN bundles as a function of temperature. Inset: Thermal conductivity (k) as a function of temperature (T). Solid and open circles represent the measurement results of the 10 nm and the 148 nm diameter SWCN bundle, respectively.

from phonon scattering at contacts between individual tubes in a bundle. The inset to Fig. 8 shows the calculated thermal conductivity values of the two bundles, which are much lower than the results that we previously obtained for an individual MWCN. We have measured very high room-temperature thermal conductivity of individual SWCNs grown by the CVD method (see Fig. 3(d)), and the measurement results will be reported elsewhere.

Figure 9 shows the measured electrical conductance of the two SWCN bundles. For the 10 nm diameter bundle, the electrical conductance shows a power law dependence of $T^{1.7}$ with temperature. On the other hand, the electrical conductance of the 148 nm bundle can be fitted using two different power law dependences, i.e., $\sim T^{1.5}$ below 60 K and $\sim T$ above. These behaviors are different from those obtained by Bockrath et al. [22] and Yao et al. [23], where a single $T^{0.6}$ dependence was observed for smaller metallic SWCN bundles in the range of 4–400 K. The $T^{0.6}$ behavior was thought to be caused by the tunneling resistance from the metal electrodes to the nanotube according to the Luttinger-Liquid model [22]. We expect that there are many defects and contacts in the two relatively large bundles that we have measured. The electrical resistance is thus dominated by scattering inside the bundle instead of tunneling from the metal contact into the SWCN.

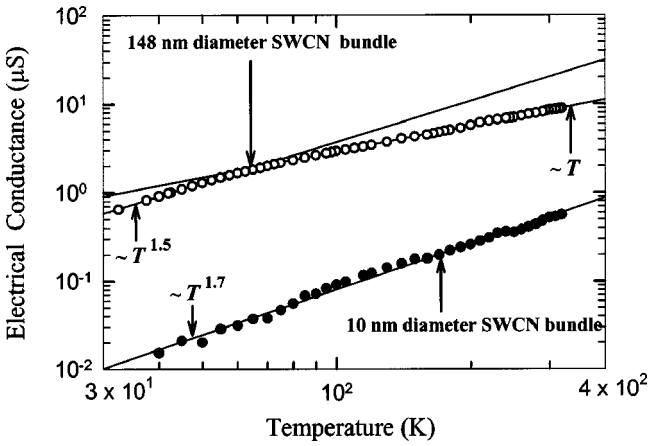

Fig. 9 Electrical conductance of two SWCN bundles as a function of temperature

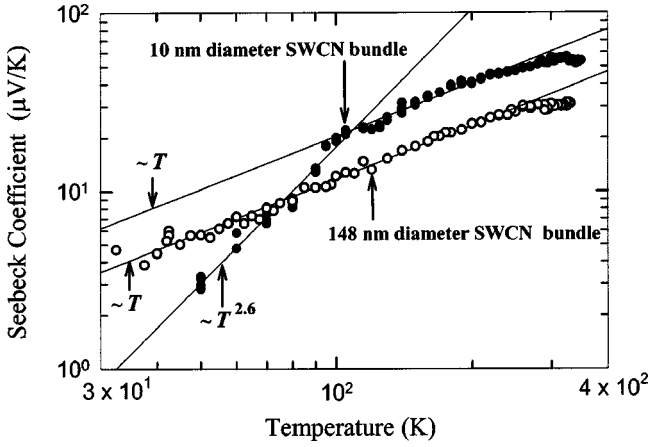

Fig. 10 Seebeck coefficient of two SWCN bundles as a function of temperature

As discovered by Collins et al. [24], the electrical conductance and Seebeck coefficient of SWCN bundles are very sensitive to oxygen exposure. Oxygen doping can result in enhanced electrical conductance of semiconducting SWCNs and hole-type majority carriers of a bundle, which usually consists of both metallic and semiconducting SWCNs. The hole doping further results in positive values of Seebeck coefficient that are much larger than that of a metal. As SWCN bundles were deoxygenated in high vacuum (10^{-6} to 10^{-8} Torr), negative values of Seebeck coefficient with smaller magnitudes than those of oxygenated samples were found [24,25].

Because large and positive values of Seebeck coefficient were observed in our measurement, as shown in Fig. 10, it is possible that the SWCN bundles were still oxygen doped, despite the fact that they were kept in vacuum for a few hours before the measurement. Note that Fig. 10 plots the difference in Seebeck coefficient between the sample and the Pt electrode, i.e., $S_s - S_{Pt}$. The magnitude of S_{Pt} is typically 5 μV/K at 300 K and decreases linearly with temperature [26], much smaller than the measurement result of $S_s - S_{Pt}$. Thus, $S_s - S_{Pt} \approx S_s$.

For the 148 nm diameter bundle, the measured Seebeck coefficient shows linear temperature dependence in the temperature range of 30–250 K, and saturates above 250 K. This bears some similarity to the measurement result of oxygen-exposed SWCN mats by Hone et al. [3], where the saturation temperature was about 100 K. The linear dependence, which is expected for a metallic sample, is also observed for the 10 nm SWCN bundle in

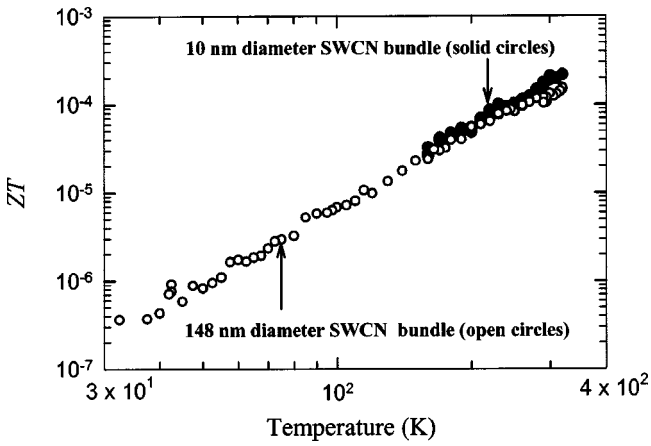

Fig. 11 Thermoelectric figure of merit (ZT) of two SWCN bundles as a function of temperature

the temperature range of 100 K to 250 K. In addition, the Seebeck coefficient for this bundle also saturates above 250 K. However, below 100 K, a power law dependence of $T^{2.6}$ is observed, indicating a departure from the metallic behavior. These observations will be analyzed elsewhere.

The thermoelectric figure of merit ($ZT \equiv S^2/RG$, where S, R, and G are Seebeck coefficient, electrical resistance, and thermal conductance of the sample) is calculated from the measurement results, and is plotted in Fig. 11. The ZT is small for the two SWCN bundles.

Conclusions

We have batch-fabricated a microdevice for measuring the thermal conductance, electrical conductance, and Seebeck coefficient of one-dimensional nanostructures including nanotubes, nanowires, and nanobelts. The measurements are performed with the sample placed in an evacuated liquid helium cryostat spanning a temperature range of 4–400 K. The sensitivity in thermal conductance measurement is estimated to be on the order of 10^{-10} and 10^{-9} W/K at 30 and 300 K, respectively. Errors due to radiation are estimated to be less than 8×10^{-14} and 7×10^{-11} W/K at 30 K and 300 K, respectively; while conduction through residual gas molecules contributes to less than 2×10^{-12} W/K at 300 K. The TCR of the PRT becomes smaller at temperatures below 30 K. To reduce the measurement uncertainty at low temperatures, one needs to use other high-TCR materials such as Nb doped Si to replace the PRT.

The measurement results of a 10 nm and a 148 nm-SWCN bundle are presented. Due to phonon scattering at many defects and contacts in the bundles, the observed thermal conductivity is low compared to that of an individual MWCN. For the 148 nm bundle, the thermal conductivity exhibits a $T^{1.5}$ in the temperature range of 20–100 K. To verify the expected linear temperature dependence of the thermal conductance of SWCNs at low temperatures, we will need to measure individual SWCNs grown by the CVD method in order to eliminate the influences from phonon scattering at contacts between individual tubes in a bundle.

Acknowledgments

For this work, LS, CY, and DK are supported by a CAREER award and an instrumentation grant from the Division of Chemical and Transport System of NSF. DL and AM are supported by the NSF NIRT program and by the Basic Energy Science program of DOE. The SnO_2 sample is provided by Prof. Z. L. Wang's group at Georgia Institute of Technology. We thank the Welch foundation for partial financial support to the Center for Nano and Molecular Science and Technology, University of Texas at Austin.

Nomenclature

A = area [m^2]
C = specific heat [J/K-m^3]
D = distance between the two membranes [m]
G = thermal conductance [W/K]
I, i = current [A]
k = thermal conductivity [W/m-K]
L = length [m]
Q = heat [W]
R = differential electrical resistance [Ω]
S = Seebeck coefficient [V/K]
T = temperature [K]
V, v = voltage [V]
σ = Stefan-Boltzmann's constant [W/m^2-K^4]

Subscripts

a = air
0 = environment
b = beam
c = contact
eq = equivalent
h = heating membrane
L = Pt lead
n = nanostructure sample
s = sensing membrane

References

[1] Volz, S. G., and Chen, G., 1999, "Molecular Dynamics Simulation of Thermal Conductivity of Silicon Nanowires," Appl. Phys. Lett., **75**, pp. 2056–2058.
[2] Khitun, A., Balandin, A., and Wang, K. L., 1999, "Modification of the Thermal Conductivity in Silicon Quantum Wires Due to Spatial Confinement of Acoustic Phonons," Superlattices Microstruct., **26**, pp. 181–193.
[3] Dresselhaus, M. S., and Eklund, P. C., 2000, "Phonons in Carbon Nanotubes," Adv. Phys., **49**(6), pp. 705–814.
[4] Schwab, K., Henriksen, E. A., Worlock, J. M., and Roukes, M. L., 2000, "Measurement of the Quantum of Thermal Conductance," Nature (London), **404**, pp. 974–976.
[5] Hone, J., Ellwood, I., Muno, M., Mizel, A., Cohen, M. L., Zettl, A., Rinzler, A. G., and Smalley, R. E., 1998, "Thermoelectric Power of Single-Walled Carbon Nanotubes," Phys. Rev. Lett., **80**, pp. 1042–1045.
[6] Yi, W., Lu, L., Zhang, D. L., Pan, Z. W., and Xie, S. S., 1999, "Linear Specific Heat of Carbon Nanotubes," Phys. Rev. B, **59**, pp. R9015–9018.
[7] Mizel, A., Benedict, L. X., Cohen, M. L., Louie, S. G., Zettl, A., Budraa, N. K., and Beyermann, W. P., 1999, "Analysis of the Low-Temperature Specific Heat of Multiwalled Carbon Nanotubes and Carbon Nanotube Ropes," Phys. Rev. B, **60**, pp. 3264–3270.
[8] Hone, J., Whitney, M., Piskoti, C., Whitney, M., and Zettl, A., 1999, "Thermal Conductivity of Single-Walled Carbon Nanotubes," Phys. Rev. B, **59**, pp. R2514–2516.
[9] Hone, J., Llaguno, M. C., Nemes, N. M., Johnson, A. T., Fischer, J. E., Walters, D. A., Casavant, M. J., Schmidt, J., and Smalley, R. E., 2000, "Electrical and Thermal Transport Properties of Magnetically Aligned Single Wall Carbon Nanotube Films," Appl. Phys. Lett., **77**, pp. 666–668.
[10] Berber, S., Kwon, Y.-K., and Tomanek, D., 2000, "Unusually High Thermal Conductivity of Carbon Nanotubes," Phys. Rev. Lett., **84**, pp. 4613–4616.
[11] Che, J., Cagin, T., and Goddard, W. A., 2000, "Thermal Conductivity of Carbon Nanotubes," Nanotechnology, **11**, pp. 65–69.
[12] Osman, M., and Srivastava, D., 2001, "Temperature Dependence of the Thermal Conductivity of Single-Wall Carbon Nanotubes," Nanotechnology, **12**, pp. 21–24.
[13] Lin, Y.-M., Sun, X., and Dresselhaus, M. S., 2000, "Theoretical Investigation of Thermoelectric Transport Properties of Cylindrical Bi Nanowires," Phys. Rev. B, **62**, pp. 4610–4623.
[14] Heremans, J. P., Thrush, C. M., Morelli, D. T., and Wu, M.-C., 2002, "Thermoelectric Power of Bismuth Nanocomposites," Phys. Rev. Lett., **88**, p. 216801.
[15] Cahill, D. G., 1990, "Thermal Conductivity Measurement From 30–750 K: The 3ω Method," Rev. Sci. Instrum., **61**, pp. 802–808.
[16] Shi, L., 2001, "Mesoscopic Thermophysical Measurements of Microstructures and Carbon Nanotubes," Ph.D. dissertation, University of California, Berkeley.
[17] Kim, P., Shi, L., Majumdar, A., and McEuen, P. L., 2001, "Thermal Transport Measurements of Individual Multiwalled Carbon Nanotubes," Phys. Rev. Lett., **87**, p. 215502.
[18] De Vecchio, D., Taborek, P., and Rutledge, J. E., 1995, "Matching the Resistivity of Si:Nb Thin Film Thermometers to the Experimental Temperature Range," Rev. Sci. Instrum., **66**, pp. 5367–5368.
[19] Li, D., Wu, Y., Kim, P., Shi, L., Mingo, N., Liu, Y., Yang, P., and Majumdar, A., 2003, "Thermal Conductivity of Individual Silicon Nanowires,"submitted.
[20] Li, D., Prieto, A. L., Wu, Y., Martin-Gonzalez, M. S., Stacy, A., Sands, T., Gronsky, R., Yang, P., and Majumdar, A., 2002, "Measurement of Bi_2Te_3 Nanowire Thermal Conductivity and Seebeck Coefficient," Proc. 21st International Conference on Thermoelectrics, IEEE, pp. 333–336.
[21] Shi, L., Hao, Q., Yu, C., Kim, D., Farooqi, R., Mingo, N., Kong, X., and Wang, Z. L., 2003, "Thermal Conductivity of SnO_2 Nanobelts," in preparation.
[22] Bockrath, M., Cobden, D. H., Lu, J., Rinzler, A. G., Smalley, R. E., Balents, L., and McEuen, P. L., 1999, "Luttinger-Liquid Behavior in Carbon Nanotubes," Nature (London), **397**, pp. 598–601.
[23] Yao, Z., Postma, H. W. Ch., Balents, L., and Dekker, C., 1999, "Carbon Nanotube Intramolecular Junctions," Nature (London), **402**, pp. 273–280.
[24] Collins, P. G., Bradley, K., Ishigami, M., and Zettl, A., 2000, "Extreme Oxygen Sensitivity of Electrical Properties of Carbon Nanotubes," Science, **287**, pp. 1801–1804.
[25] Bradley, K., Jhi, S.-H., Collins, P. G., Hone, J., Cohen, M. L., Louie, S. G., and Zettl, A., 2000 "Is the Intrinsic Thermoelectric Power of Carbon Nanotubes Positive?" Phys. Rev. Lett., **85**, pp. 4361–4364.
[26] Rowe, D. M., 1995, *CRC Handbook of Thermoelectrics*, CRC Press, New York.